The 30 m Small-Angle Neutron Scattering Instruments at the National Institute of Standards and Technology

C. J. GLINKA,* J. G. BARKER, B. HAMMOUDA, S. KRUEGER, J. J. MOYER† AND W. J. ORTS‡

NIST Center for Neutron Research, National Institute of Standards and Technology, Gaithersburg, Maryland 20899, USA. E-mail: cglinka@nist.gov

Abstract

Two high-resolution, general-purpose, small-angle neutron scattering instruments have been constructed at the National Institute of Standards and Technology's Center for Neutron Research. The instruments are 30 m long and utilize mechanical velocity selectors, pinhole collimation and high-data-rate two-dimensional position-sensitive neutron detectors. The incident wavelength, wavelength resolution and effective length of the instruments are independently variable, under computer control, and provide considerable flexibility in optimizing beam intensity and resolution. The measurement range of the instruments extends from 0.0015 to 0.6 Å^{-1} in scattering wavevector, corresponding to structure in materials from 10 Å to nearly 4000 Å. The design and characteristics of the instruments, and their modes of operation, are described, and data are presented which demonstrate their performance.

1. Introduction

Small-angle neutron scattering (SANS) instruments which utilize long flight paths, long-wavelength neutrons from a 'cold source' and position-sensitive counters have been in operation since the 1970s. They were developed in Germany at Jülich (Schelten, 1972) and in France at Grenoble (Ibel, 1976), and are still the most effective type of SANS instrument for probing structure in materials in the range from roughly 10 to 4000 Å. Two SANS instruments of this type, each 30 m in overall length, have been constructed at the 20 MW research reactor at NIST's Center for Neutron Research (NCNR). The NCNR's cold neutron source and 60 × 30 m neutron-guide hall provide, for the first time at a US research reactor, optimal conditions for long-flight-path, pinhole collimation SANS.

The two 30 m SANS instruments at the NCNR are nearly identical and were designed to be versatile, user-oriented instruments that would incorporate, and in some cases improve upon, the best features of existing instruments. To these ends, both instruments have: (i) high-transmission, multidisk mechanical velocity selectors with variable speed and pitch to allow both the mean wavelength and the wavelength spread of the incident beam to be varied over a wide range; (ii) an evacuated pre-sample flight path with neutron-guide sections that can be readily shifted in or out of the beam to vary the beam divergence and flux on the sample by changing the effective source-to-sample distance; (iii) two choices of sample location (*a*) a permanently installed evacuable sample chamber with a computer-controlled translation stage, or (*b*) a 600 mm diameter sample table, between the pre-sample flight path and the main sample chamber, to accommodate large pieces of apparatus such as electromagnets, cryostats, furnaces, shear cells, *etc.*; (iv) a large (640 × 640 mm with 10 mm resolution), high-data-rate two-dimensional position-sensitive detector which moves along rails in an evacuated post-sample flight path to vary the sample-to-detector distance and, in addition, moves transversely to the beam direction (up to 250 mm) to extend the *Q* range covered at a particular detector distance; (v) separate data acquisition systems which provide computer control of the complete instrument configuration and sample environment through a user-friendly, menu-driven computer interface. A color monitor displays a continuously updated image of the data being collected and completed data-sets can be reduced online.

The measurement range of the instruments extends from 0.0015 to 0.6 Å^{-1} which corresponds to structural features in materials ranging in size from roughly 10 to 4000 Å. The characteristics of the SANS instruments are summarized in Table 1 and Fig. 1 shows a schematic diagram of the instrument.

The two SANS instruments differ primarily in their sources of support and resulting allocation of beam time. The 30 m SANS instrument on neutron guide NG-7, in operation since May 1991, was developed jointly by NIST, the Exxon Research and Engineering Company and the University of Minnesota who constitute one of the participating research teams (PRT) at the NCNR. Up to 75% of the beam time on this instrument is available to the members of the PRT. The remaining

---

Table 1. *Characteristics of the 30 m SANS instruments*

Source	Neutron guide (NG-3) 60 × 60 mm Neutron guide (NG-7) 50 × 50 mm
Monochromator	Mechanical velocity selector with variable speed and pitch
Wavelength range	5.0–20 Å
Wavelength resolution	10–30% $\Delta\lambda/\lambda$ (FWHM)
Source–sample distance	4.0–16 m in 1.5 m steps *via* insertion of neutron-guide segments
Sample–detector distance	1.3–13.2 m continuously variable for NG-3 1.0–15.3 m continuously variable for NG-7
Collimation	Circular pinhole collimation
Sample size	5–25 mm diameter
Q range	0.0015–0.6 Å^{-1}
Size regime	10 to ~4000 Å
Detector	640 × 640 mm multiwire ^{3}He position-sensitive proportional counter (10 × 10 mm resolution)
Ancillary equipment	Automatic multi-specimen sample changer with temperature control from 263 to 473 K Electromagnet (0 to 1.5 T) Couette-type shearing cell Pressure cell (< 10^8 Pa, 298–433 K)

25% is distributed by the NCNR's Program Advisory Committee to researchers who submit experiment proposals that undergo peer review. The construction and operation of the 30 m SANS instrument on neutron guide NG-3, in operation since September 1992, has been supported by the National Science Foundation (NSF) through its Center for High Resolution Neutron Scattering (CHRNS) at the NCNR. In return for this support, 75% of the beam time on this instrument is allocated to approved experiment proposals. The remaining 25% is set aside for use by the staff scientists responsible for the instrument.

In the following sections, the design of the 30 m SANS instruments and associated data acquisition systems is described in detail and data are presented which illustrate the performance of individual components and the instrument overall. Also discussed are procedures for carrying out SANS measurements, calibrating the instruments and determining absolute cross sections.

2. Instrument components and characteristics

2.1. *Neutron source and beam guides*

The NIST research reactor is a 20 MW, heavy-water-moderated and heavy-water-cooled reactor. It has a unique split-core design, with parts of the fuel above and below a 17 cm gap. The beam tubes, which emanate radially from the gap, thus see a somewhat lower level of γ and fast neutron radiation. At 20 MW, the isotropic thermal neutron flux in the core of the reactor is 4 × 10^{14} n cm^{-2} s^{-1} and approximately 2 × 10^{14} n cm^{-2} s^{-1} at the inner tips of the beam tubes. The thermal neutron spectrum is approximately Maxwellian at a temperature of ~ 350 K.

The NIST reactor was designed with provision for a large-volume cold neutron moderator. In 1987 the reactor's first cold moderator, a 16 l block of D_2O ice cooled to 40 K, went into operation. The spectrum from this source, for wavelengths > 3 Å, was approximately Maxwellian with a temperature of 65 K and produced an enhancement in flux, relative to the thermal beam tubes, of between 2.5 and 4 for wavelengths from 5 to 10 Å, respectively. Some of the measurements in this paper on the performance of the SANS instruments were made while the D_2O ice source was in operation. The D_2O ice source has since been replaced by an improved liquid-hydrogen moderator and a higher-capacity helium-gas refrigeration system. The geometry of the new source, which permits it to be located closer to the reactor core, and its lower operating temperature (20 K with an approximately Maxwellian spectrum temperature of 30–35 K) have increased the flux by factors of 3.5 to 6 for wavelengths between 5 and 12 Å, respectively, relative to the D_2O ice source. The new source has been in operation since October 1995.

Seven straight neutron-guide tubes channel neutrons from the cold source to the instruments in the 60 × 30 m neutron-guide hall that was built adjoining the reactor in 1989. The NG-7 and NG-3 guide tubes which supply the 30 m SANS instruments are coated internally with a thin layer of ^{58}Ni and have estimated transmission losses of about 1–2% m^{-1}. The NG-7 guide is 50 mm wide by 120 mm high at the cold source, though only 50 × 50 mm continues to the entrance to the NIST-PRT SANS
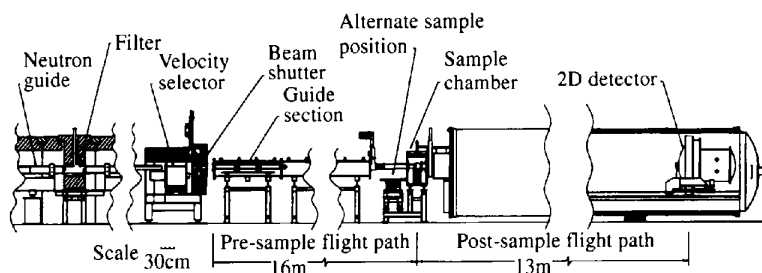

Fig. 1. A schematic diagram of the NG-3 30 m SANS instrument.

instrument, 45 m from the cold source. The NG-3 guide is 60 × 150 mm at the source and 60 × 60 mm at the CHRNS SANS instrument, 35 m from the source.

2.2. Beam filtering

The neutron guides for the SANS instruments each have filters, as indicated schematically in Fig. 1, to remove core γ rays and fast neutrons from the beam. The filters consist of up to 200 mm of high-purity (99.999+% Bi) bismuth, in the form of large (several tens of mm on a side) randomly oriented single-crystal grains, and 200 mm of vacuum-cast, polycrystalline beryllium (Glinka et al., 1986), cooled to 77 K in a liquid-nitrogen cryostat. The filtered beams have negligible γ-ray contamination and all wavelengths longer than 4.0 Å, the Bragg cut-off for beryllium. The measured transmission, at 77 K, of one of these filters, consisting of 150 mm Bi and 150 mm Be at the time of the measurements, was 80% at 10 Å and decreased at both longer and shorter wavelengths: to ~75% at 15 Å because of increased absorption and to ~70% at 5 Å because of Bragg scattering below the Bragg cut-off for bismuth (7.9 Å).

2.3. Wavelength selection

The neutrons which emerge from the filtered guide preceding each SANS instrument are mechanically monochromated by passing through a multidisk neutron velocity selector. The selector has a set of slotted disks that are spaced and phased along an axle to form helical pathways. The rotational frequency of the selector's rotor (axle with disks) determines the mean wavelength of the quasi-continuous beam transmitted by the selector. The physical specifications and corresponding performance parameters for the selectors are given in Table 2. The rotor and its evacuated housing are mounted on a bearing which allows the selector to be rotated about a central vertical axis to incline the rotor axis to the beam direction. Tilting the rotor axis with respect to the beam direction changes the effective pitch of the helical pathways as well as the wavelength bandpass, $\Delta\lambda/\lambda$, where $\Delta\lambda$ is the FWHM (full width at half-maximum) of the outgoing wavelength distribution and λ is the mean transmitted wavelength. The bandpass of the selectors can be varied from 0.10 to 0.30 corresponding to tilt angles from 3° to −3°.

The multidisk velocity selectors used on the 30 m SANS instruments were developed (Rosta et al., 1987; Rosta, 1989) and manufactured in Hungary. The expected performance of these selectors has been analyzed by Hammouda (1992) and Copley (1993). Their actual performance has been determined by directly measuring the time-of-flight distribution of the neutrons transmitted by the selectors as a function of rotation frequency and angle of inclination to the beam collimation. Fig. 2 shows some representative wave-

Table 2. *Characteristics of the Hungarian model MDR-13-410-420 multidisk velocity selectors used on the 30 m SANS instruments*

Rotor physical parameters

Rotor length	420 mm
Disk diameter	410 mm
Pitch angle of helical pathways, α	17°
Disk slot opening angle, β (slot width/slot radius)	2.25°
Neutron absorber	Gadolinium oxide
Rotation frequency	0–6000 r min^{-1}

Nominal performance characteristics

Transmission† of selected wavelength, λ_o	75%
Beam size	50 × 50 mm
Beam divergence (disk slot width/rotor length)	0.9°
Rotor axis tilt angles, δ	$-4° \leq \delta \leq 4°$
Resolution,‡ $\Delta\lambda/\lambda_o$	
Rotor tilt angle, $\delta = 0$	13%
Rotor tilt angle, $\delta = +3°$	9%
Rotor tilt angle, $\delta = 3°$	23%

† Ratio of slot width to slot spacing. ‡ $\Delta\lambda/\lambda_o = (\beta/\alpha)/[1 + 0.141\delta(°)]$.

length distributions determined by time of flight for three selector tilt angles. The measured widths of the distributions are somewhat larger than the calculated values, neglecting beam divergence, given in Table 2. Because of the λ^2 dependence of the scattering cross section, $d\Sigma/d\Omega$, the $\lambda_{r.m.s.} = (\langle\lambda^2\rangle)^{1/2}$ values are calculated from the measured distributions and used to generate a calibration curve of $\lambda_{r.m.s.}$ *versus* selector frequency for each tilt angle.

Immediately following the velocity selector, a low-efficiency ($\sim10^{-5}$) fission counter monitors the intensity of the monochromatic beam. During data collection intervals, which are specified in s, the monitor counts accumulate in a separate counting channel. Completed data-sets are then normalized to a fixed number of monitor counts, which corresponds to a fixed number of neutrons incident on the sample regardless of any variation in the reactor power or cold source temperature during the measurement.

2.4. Beam collimation

The monochromated beam is collimated by circular apertures inside the 15 m long pre-sample flight path of each SANS instrument. The flight path consists of ten identical 1.5 m long sections (see Fig. 1), rectangular in cross section (760 mm wide × 300 mm high), which form one extended vacuum enclosure for the incident beam. Each section, shown in cross section in Fig. 3, has an external stepping-motor-driven linear actuator that controls the positioning of a transverse-motion table inside. The tables in the first eight sections following the velocity selector have neutron-guide elements, 1.5 m

long with 50 × 50 mm cross sections, mounted alongside 50 mm diameter beam apertures. By inserting guide elements into the beamline, the effective source-to-sample distance can be changed from 4 to 16 m in 1.5 m increments to vary the beam divergence and flux on the sample. The last guide inserted is immediately followed by a source-defining, 50 mm diameter aperture made from a casting of lithium-6 carbonate in epoxy. When no guides are inserted (16 m source-to-sample distance), the source aperture size can be chosen to be either 38 or 22 mm. The definition of the incident-beam collimation is completed by the choice of circular beam aperture at the sample position.

At the junctions between the flight-path sections, 25 mm thick panels of lithium-loaded polyethylene (7%

lithium by weight) with square beam openings provide shielding in the forward direction from the beam diverging from the source aperture. The openings in the panels, which are not beam defining, have 3° tapers to reduce scattering and reflection from the edges (see Fig. 3). The central sections of the panels which intercept most of the stray radiation are constructed from a flexible ^{6}LiF polymer composite material (70% ^{6}LiF by weight) backed on the downstream side by 0.125 mm thick cadmium. This construction represents a compromise in trying to minimize γ radiation due to neutron capture, by using a neutron absorber, lithium-6, that is not a γ emitter, while also minimizing parasitic scattering which degrades the beam definition through the use of a low-albedo material, cadmium.
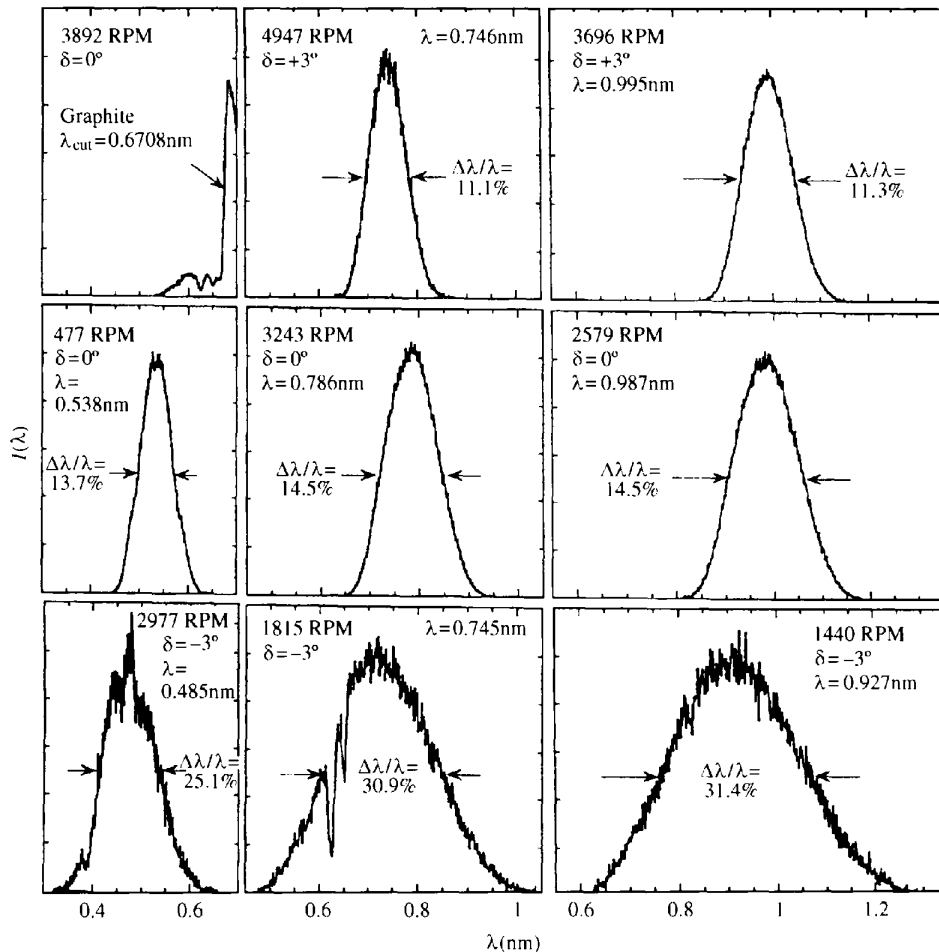

Fig. 2. The distribution of wavelengths in the incident beam, as measured by time of flight, for various rotational speeds and selector tilt angles for the velocity selector on guide NG-7. The upper left-hand figure corresponds to a measurement in which a 75 mm thick block of graphite was inserted into the beam. The position of the sharp edge corresponds to the Bragg cut-off for graphite at 6.708 Å. The remaining figures on the top, middle and lower rows correspond to 3°, 0° and −3° selector tilt angles, respectively. All wavelengths, λ, are root-mean-square average values: $\lambda_{r.m.s.} = \lambda_0[1 + (\sigma_\lambda/\lambda_0)^2]^{1/2}$, where λ_0 is the mean and σ_λ the standard deviation of the wavelength distribution. An effective FWHM value is calculated assuming the distribution is Gaussian in shape: $\Delta\lambda/\lambda_0 = 2.355\sigma_\lambda/\lambda_0$. Bragg scattering from oriented bismuth crystals produces dips in the distribution at 6.3 and 6.7 Å as seen in the lower center figure. The reduced FWHM for the lower left figure is caused by the Bragg cut-off for beryllium at $\lambda_{cut} = 4.0$ Å.

2.5. Sample stage

The SANS instruments have two sample locations: (i) a permanently installed evacuable sample chamber with a computer-controlled translation stage and (ii) a 600 mm diameter rotary table, between the pre-sample flight path and the main sample chamber, to accommodate large pieces of apparatus such as electromagnets, cryostats, furnaces, or shear cells, for example. When the sample chamber is used, a lightweight tube bridges the sample table (see Fig. 1) to extend the pre-sample vacuum flight path up to the chamber. When the sample table is used, the bridging tube is removed and the sample chamber is evacuated to become, in effect, part of the post-sample flight path, thereby increasing the minimum sample-to-detector distance by approximately 0.5 m. The sample chamber may be used under vacuum, open to the air or filled with an inert gas. When not evacuated, single-crystal beam windows (sapphire before the sample and silicon after) mounted on various length adapters inside the chamber minimize air space in the beam path.

2.6. Post-sample flight path and detector carriage

The post-sample flight path is a 1.7 m diameter cylindrical vacuum vessel constructed from 9.5 mm thick aluminium with external reinforcing rings at 1.5 m intervals. The vessel is lined with 0.5 mm cadmium sheet and covered with 50 mm of paraffin and borax (50/50 mixture by volume) cast in 1.5 m long sections of thin-wall, rectangular-cross-section tubes which are stacked around the circumference of the vessel between the reinforcing rings. A stepping-motor-driven carriage moves along rails inside the vessel to vary the sample-to-detector distance continuously from 1.3 m (1.0 m) to 13.2 m (15.3 m) for the NG-3 (NG-7) instrument. The detector carriage also moves transversely to the beam direction up to 250 mm to extend the Q range covered at a particular detector distance. Mounted on the carriage is an independent xy stage for positioning any of four

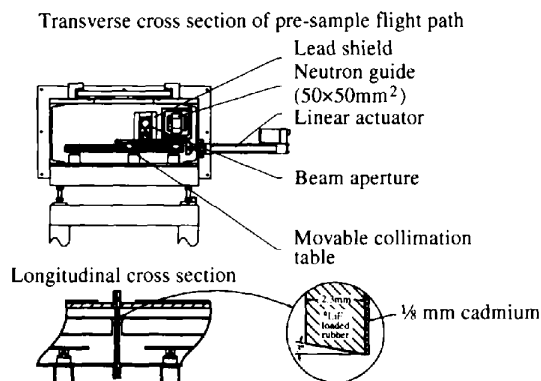Transverse cross section of pre-sample flight path

Fig. 3. Transverse and longitudinal cross-sectional schematic diagrams of the pre-sample flight path of the 30 m SANS instruments.

Table 3. *Characteristics of the CERCA model XYP 64 × 64-10 multiwire proportional counters used on the 30 m SANS instruments*

Physical characteristics

Active area	640 × 640 mm
Active depth	25 mm
Gas mixture	2 × 10⁵ Pa, helium-3; 0.4 × 10⁵ Pa CF₄
Anode	64 Cu–Be alloy wires, 10 mm spacing
Cathodes	66 Cu–Be wire bands (nine per band); 10 mm spacing
Aluminium window	5.2 mm (4 mm dome, 1.2 mm diaphragm)

Performance characteristics

	Measured	Manufacturer's specifications
Spatial resolution	10 × 10 mm	10 × 10 mm
Detection efficiency at 0.5 nm	80%	60%
Detection dead time per event	2–3 µs	4 µs
Maximum count rate		
Per pixel	>10³ counts s⁻¹	10⁴ counts s⁻¹
Entire detector	5% lost counts at 1.3 × 10⁴ counts s⁻¹	10⁵ counts s⁻¹
Gas multiplication factor	~110–150†	~30–50†
Background noise‡	1–2 h⁻¹ pixel⁻¹	<1 h⁻¹ pixel⁻¹

† G. Marx and J. Jacobé, private communication.   ‡ Count rate with reactor off.

choices of circular beam stops, ranging from 50 to 100 mm in diameter, in front of the detector. Beam stops made from a boron carbide/aluminium composite material or a ⁶Li-loaded silicate glass have been found to be equally effective in stopping the unscattered beam without producing any detectable background in the counter.

2.7. Two-dimensional position-sensitive detector

The two-dimensional position-sensitive neutron detectors used on the SANS instruments are commercial multiwire proportional counters (MWPC) (Model XYP 64 × 64-10, manufactured by CERCA, Romans, France) of the type developed at the Institut Laue–Langevin (ILL) (Allemand *et al.*, 1975; Jacobe *et al.*, 1983). The physical and performance characteristics of these detectors are given in Table 3. The counter has three planes of parallel wires, a central anode wire plane and two orthogonal cathode wire planes, each with a 10 mm spacing between adjacent wires. The spatial resolution function, measured with a collimated beam incident on a 1 mm aperture in front of the detector, is approximately Gaussian with an FWHM = 10 mm in both directions. There is a separate charge-sensitive preamplifier and amplifier for each cathode wire to register the charge induced in the vicinity of the electron avalanche which occurs on an anode wire as a result of each neutron capture in the counter. The first amplifier signal from

each cathode plane that crosses a preset threshold level determines the coordinate assigned to the position of the captured neutron. A coincidence circuit verifies that a threshold crossing occurs on both the X and Y cathodes within a preset interval (typically 100 ns) before sending the digitized event coordinates to the data acquisition system. The principal advantages of this detection scheme are: (i) the position encoding is inherently linear (one pixel per 10 mm); and (ii) the count-rate capacity is high because of a short signal-processing time, a consequence of the low input capacitance ($\sim$100 pF) per amplifier which results from subdividing the cathodes into individual counting circuits.

The operating characteristics of the MWPC depend on the high voltage setting, which determines the amount of charge deposited on the anode per event, the gain setting of each of the 128 cathode wire amplifiers and the amplifier threshold levels (one per 32 amplifiers) which screen out low-level electronic noise. One criterion for selecting these operating parameters is the overall absolute detection efficiency of the MWPC which should approach 85% for 5 Å neutrons based on the ^{3}He filling pressure (202.65 kPa) and the active depth (25 mm) of the counter. When tuned to maximize detection efficiency, however, variations in the electronic background level (count rate in the absence of neutrons) and the point-to-point (relative) efficiency of the MWPC have been observed to occur on time scales of hours which is unacceptable. By raising the amplifier threshold levels, it has been possible to stabilize the response of the MWPC over periods of days to weeks, but with a resulting reduction in detection efficiency to about 60% at 5.0 Å.

The gain settings for the individual cathode wire amplifiers are adjusted to make isotropic scattering, typically the small-angle scattering from a 1 mm thick sample of H_2O, appear as uniform as possible over the entire detector (after correcting for the small variation in the solid angle subtended by each pixel because of the planar geometry of the detector). This is an iterative process in part because adjusting the gain of one amplifier affects the apparent response of adjacent wires as a result of the threshold-crossing scheme used to determine event positions. With patience, a reasonably uniform detector response can be achieved. Fig. 4 shows a representative result for the isotropic scattering from water. To remove the residual variations in the relative efficiency of the MWPC, data-sets are routinely divided, pixel by pixel, by a pattern like that in Fig. 4 which is measured (with at least 10^4 counts per pixel) at least every few weeks.

Serious failures, requiring disassembly of the counters, have occurred in two of the three MWPCs purchased for the SANS instruments in less than 2 years of operation. In one case, the efficiency in a roughly 50 × 30 mm region of the detector, outside any area that could have been exposed even accidentally to the direct beam, dropped to nearly zero in the course of a few hours. Neither the cause nor the nature of this failure has been satisfactorily explained. In the other case, one cathode wire suddenly ceased to function. Disassembly of that counter revealed that the wire had become short-circuited by a metal sliver in the counter which had, over time, penetrated a thin strip of kapton insulation.

There have been a number of problems with the detector electronics as well. One persistent problem, which we have not been able to correct, becomes apparent when measuring scattering that is highly localized on the detector, such as Bragg peaks from colloidal crystals, for example. In such cases, weak false images of the true scattering spot(s) may appear at positions shifted either horizontally or vertically due to misencoding of either the x or y coordinates of a detected neutron's real position. The misencoded locations correspond to wires whose preamplifier/amplifier circuits are noisier than average. Noise pulses on these wires can be mistaken for a detected neutron if they occur in coincidence with a pulse from a wire from the other cathode. This problem is inherent in the design of the detector electronics which provides only one discriminator setting per 32 amplifier circuits to screen out noise.

2.8. Data acquisition system

The MWPC electronics provide a 12 bit digitized position for each detected neutron along with two signal lines that are used to control direct access to an external, CAMAC-based histogramming memory. Several memory modules are available to enable time-resolved measurements by cycling through a set of memory banks on a preprogrammed time schedule (minimum available dwell time = 100 ms). The contents of the histogramming memory are transferred approximately every 10 s to the main data acquisition computer and to a color display terminal to update a color-coded two-dimensional image of the data being collected. At the end of each counting interval, the data are written to a binary file on the computer's hard disk where they are available for online analysis while data collection proceeds. The number of counts recorded in the instrument's beam monitor scaler is also stored in the data file along with information identifying the sample, its environmental conditions and the configuration of the instrument.

Configuring the instrument and collecting data are controlled from a computer terminal at the instrument through a menu-driven user interface which provides brief on-screen explanations of all menu items. RS-232 communication lines are used to interface with motor controllers, linear actuators for the moveable neutron guides, the speed control for the velocity selector, temperature controllers, etc., which provides full automatic control over the instrument and sample environ-

ment. A series of measurements, including changes to the configuration of the instrument between runs, can be programmed to run automatically. The data collected each day are automatically archived on a removable-cartridge, magneto-optical disk drive on the instrument's computer.

3. Instrument operation and performance

3.1. *Optimal instrument configuration*

Configuring one of the 30 m SANS instruments for a particular measurement involves choosing the incident wavelength, λ, the wavelength resolution, $\Delta\lambda/\lambda$, the source-to-sample distance, L_1, the sample-to-detector distance, L_2, the size of beam stop, of diameter B_s, and the sample aperture radius, R_2. The source aperture radius, R_1, on these instruments, for reasons that will become clear below, is fixed at its maximum value, R_{1max} = 25 mm, whenever $L_1 < L_{1max}$ = 16 m, but can be chosen to be smaller, $R_1 < R_{1max}$, when $L_1 = L_{1max}$ to

provide the narrowest possible incident-beam divergence. Of course, not all of these parameter choices are independent; the beam stop (B_s = 50, 75, or 100 mm), for example, must be at least as large as the penumbra of the beam at the detector (B_{smin}) given by

$$B_{smin} = (2L_2/L_1)(R_1 + R_2) + 2R_2. \qquad (1)$$

In this section, we summarize some of the criteria that should be considered in choosing an instrument configuration, recognizing that no one set of criteria will apply to all situations.

We consider first the general criterion of maximizing the intensity in the detector corresponding to a fixed scattering vector $Q = (4\pi/\lambda)\sin(\theta/2)$ and Q resolution, where θ is the scattering angle. For the case of azimuthally symmetric small-angle scattering, the intensity (counts s^{-1}) in the detector, $I(Q)$, depends on the instrument configuration according to

$$I(Q) \propto C_D = (R_1^2 R_2^2 R\Delta R\Delta\lambda/\lambda)/(L_1^2 L_2^2 \lambda^4) \qquad (2)$$
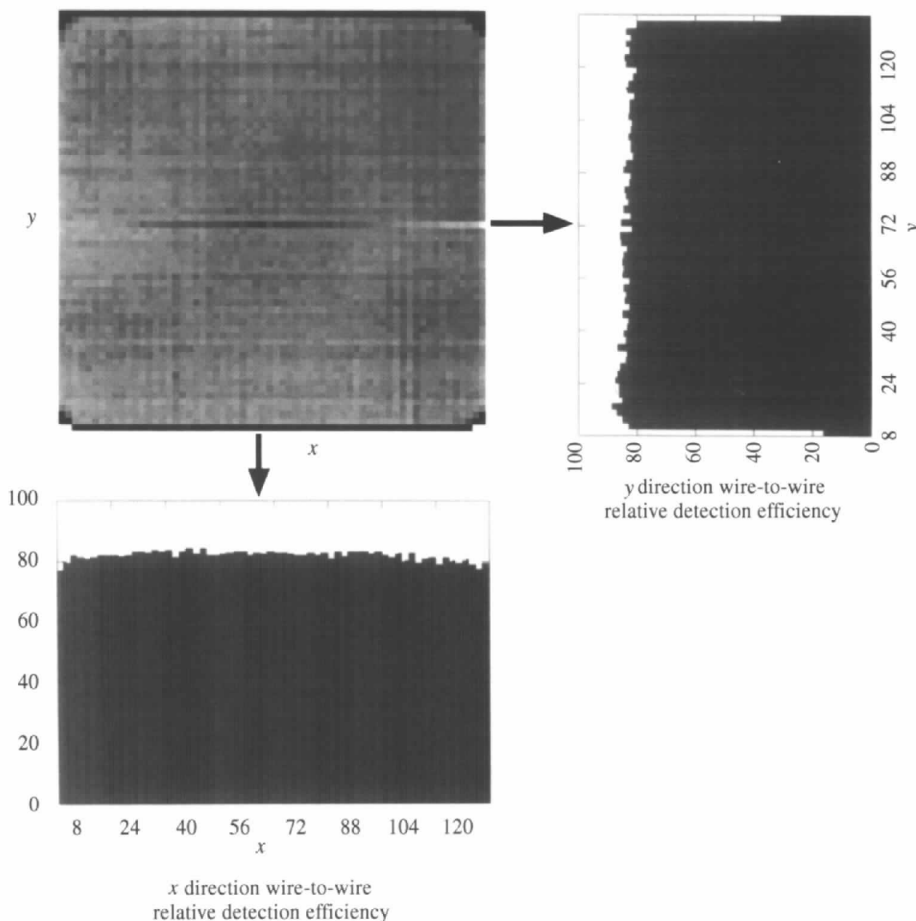
Fig. 4. A gray-scale image of the distribution in neutron intensity from an isotropic scatterer over the surface of one of the two-dimensional detectors used on the SANS instruments (lighter regions correspond to higher recorded intensity). The histograms are horizontal and vertical projections of the data which show the wire-to-wire variation in the relative detection efficiency that is typical for this type of counter.

where R is the radius of the annulus, of width ΔR, at the detector corresponding to $Q \simeq 2\pi R/\lambda L_2$. In (2) we assume that the wavelength λ is sufficiently large to lie in the Maxwellian tail of the neutron distribution where $I(\lambda) \propto 1/\lambda^5$ (Ibel, 1976). One measure of the resolution is the variance, σ_Q^2, of the magnitude of Q. The wavelength spread and angular divergence of the beam contribute independently to the variance in Q and, therefore,

$$\sigma_Q^2 = k^2 \sigma_\theta^2 + Q^2(\sigma_\lambda^2/\lambda^2) \qquad (3)$$

where $k = 2\pi/\lambda$ and the angular variance, σ_θ^2, is given by (Mildner & Carpenter, 1984)

$$\sigma_\theta^2 = (1/12)\{3(R_1/L_1)^2 + 3R_2^2[(1/L_1) + (1/L_2)]^2$$
$$+ (\Delta R/L_2)^2\}. \qquad (4)$$

Using the method of Lagrange multipliers to optimize C_D with Q and σ_Q fixed, it follows that (Mildner & Carpenter, 1984; Schmatz et al., 1974)

$$R_1/L_1 = R_2[(1/L_1) + (1/L_2)] = (2/3)^{1/2}(\Delta R/L_2)$$
$$= 2/(3^{1/2})[(R\Delta\lambda)/(L_2\lambda)] \qquad (5)$$

where we have used $\sigma_\lambda^2 = 1/6\Delta\lambda^2$ for the approximately triangular wavelength distribution ($\Delta\lambda$ = FWHM) produced by the velocity selector. The first equation in (5) implies that the source and sample radii are proportional to their distance from the detector and, therefore, define a cone that converges to a point at the detector (cone rule). Thus the optimal geometry is one that produces a (nearly) triangular beam profile at the detector, whereas for all other distances from the sample it is trapezoidal. Because of the number of parameters involved, however, the relations in (5) are not sufficient to determine completely the optimal configuration of the instrument without invoking some additional constraint.

The relations in (5) can be combined with (3) and (4) to express the detector count rate, C_D, in (2) as (May, 1994)

$$C_D \propto \sigma_Q^4 R_2^2. \qquad (6)$$

Equation (6) emphasizes the basic, yet sometimes overlooked, result that of all possible instrument configurations which yield the same Q resolution, the one that maximizes the sample size gives the highest detector count rate. Endeavoring to maximize C_D by maximizing the sample size is the additional constraint needed to complete the determination of an optimal instrument geometry. The effect of this constraint on the primary and secondary flight-path lengths, L_1 and L_2, respectively, can be seen by using (4) and (5) to express R_2 in terms of the total length of the instrument, $L_o = L_1 + L_2$, and the ratio $x = L_1/L_2$ (May, 1994)

$$R_2 = (8/5)^{1/2}\sigma_\theta L_o[x/(1 + x)^2]. \qquad (7)$$

Since the resolution, and hence σ_θ, is considered fixed, maximizing R_2 implies using the instrument at its maximum length, $L_{o\max}$, with $L_1 = L_2$ since the last term in (7) has a maximum when $x = 1$. It then follows from the cone rule [the first equation in (5)], that $2R_{2\max} = R_{1\max}$. This is the commonly used equal-flight-path configuration which is the optimal choice provided that large samples are available such that the condition $2R_2 = R_{1\max}$ can be satisfied. For the NCNR SANS instruments, the condition $2R_2 = R_{1\max} = 25$ mm in diameter which, according to (1), then requires that the 100 mm diameter beam stop be used. If the required Q resolution (or minimum Q value) cannot be achieved with this sample size, then either the wavelength should be increased or, equivalently in terms of the effect on C_D, the source and sample apertures should be reduced proportionally to maintain $R_1 = 2R_2$ to minimize the reduction in detector count rate.†

When the condition $R_2 = R_{2\max} = R_{1\max}/2$ (and, therefore, $L_1 = L_2$) is satisfied, and it is desirable or necessary to relax the resolution (i.e. increase σ_Q to increase the count rate C_D or to extend the Q range covered by the detector), (7) further implies that this should be performed by reducing L_1 and L_2 by equal amounts to reduce L_o and keep $L_1 = L_2$.

Next we consider how the above conclusions change when the available sample size is less than optimum, i.e. $R_2 < R_{1\max}/2$. Since $R_2 < R_{2\max}$, the optimum configuration is again indeterminate until an additional constraint is imposed. If, for example, the total length, L_o, is chosen to be no longer than required to achieve a desired resolution, then it has been shown (Mildner & Carpenter, 1984; May, 1994) that the symmetric configuration, $L_1 = L_2$ with $R_1 = 2R_2 < R_{1\max}$, is again optimal. However, a better choice of constraint, as pointed out by Falcão et al. (1994), is to require that $R_1 = R_{1\max}$. The cone rule, rewritten as $R_{1\max} = R_2(1 + x)$, then requires that $x > 1$, or $L_1 > L_2$. For such an asymmetric configuration of the instrument, the total length is greater than in the symmetric case for the same resolution and detector count rate as can be seen by substituting (7) into (6), which gives

$$C_D \propto \sigma_Q^4 \sigma_\theta^2 L_o^2[x^2/(1 + x)^4]. \qquad (8)$$

The last term in (8) has a maximum for $x = 1$ and, therefore, for the same C_D and σ_Q, $L_o(x > 1) > L_o(x = 1)$. More importantly, however, the secondary flight path in the asymmetric case, $L_2(x > 1) = (1/2)(1 + 1/x)L_2(x = 1)$, is shorter than in the symmetric case. Hence for the same detector count rate, Q resolution and sample size, the asymmetric configuration covers a wider Q range (for a given detector size), a significant performance

---

† Since it is generally necessary for practical considerations that the sample location be fixed, the requirement that $L_1 = L_2$ when the instrument is used at its maximum length implies that the sample location should be at the midpoint of the instrument.

advantage over the symmetric configuration. Furthermore, by using the same source size, R_{1max}, for all values of L_1, the asymmetric configuration obviates the need for multiple source apertures for every possible value of L_1, a distinct practical advantage. For these reasons the maximum source aperture size is used on the NCNR SANS instruments and an asymmetric configuration is typically used whenever the sample radius is less than $R_{1max}/2$.

With the source and sample apertures, size of beam stop and the path-length ratio, $x = L_1/L_2$, determined from the above considerations, the choices of wavelength, λ, wavelength resolution, $\Delta\lambda/\lambda$, and total instrument length, L_o, remain to complete the configuration of the instrument. The choices of λ and L_o affect most directly the accessible Q range. The minimum accessible Q value, $Q_{min} \simeq k\theta_{min}$, for example, can be expressed using (1) and (5) as

$$Q_{min} \cong (2\pi/\lambda)[(B_s/2)/L_2] = (4\pi/\lambda)(R_1/L_1)$$
$$= (4\pi/\lambda)(R_2/L_o)[(1 + x)^2/x]. \quad (9)$$

Similarly, from (2) and the cone rule, which can be expressed as $L_1 = L_o x/(1 + x)$ or $L_2 = L_o/(1 + x)$, it follows that $C_D \propto 1/(L_o^4\lambda^4)$. Hence if the neutron source has a truly Maxwellian wavelength distribution, changing λ or L_o affects the Q range and the detector count rate in the same way, in principle. In practice, however, other factors enter which break this symmetry. For example, beam filters and beam windows all have finite absorption cross sections which are proportional to λ. As a result, the long wavelength flux at the sample position drops faster than $1/\lambda^4$, perhaps as $1/\lambda^5$. The total coherent scattering from the sample which is the objective of the measurement also depends on λ, usually as λ^2, meaning that for a sample of a given thickness, a larger fraction of the incident beam is scattered when a longer wavelength is used. This dependence on wavelength can be beneficial if the scattering is weak. However, in just those cases where lower Q measurements are most needed, because the scattering is rising steeply as Q decreases and has not reached its low-Q limit, increasing λ to reduce Q_{min} can result in multiple scattering that vitiates the measurement. Hence, both to avoid multiple scattering and minimize intensity losses due to absorption, minimizing λ and maximizing L_o, consistent with the required Q range, are usually preferable.

A number of factors also affect the choice of wavelength spread $\Delta\lambda/\lambda$. There is no strict criterion for choosing $\Delta\lambda/\lambda$ since any particular choice of $\Delta\lambda/\lambda$ can satisfy the optimization condition given by the last equation in (5) at only one value of Q. For example, from (5) optimally $\Delta\lambda/\lambda = 3^{1/2}/8 \, B_s/R$; therefore at Q_{min} ($R = B_s/2$), $\Delta\lambda/\lambda = 0.43$, whereas at $R = 320$ mm, the edge of the detector, with a beam stop $B_s = 100$ mm, $\Delta\lambda/\lambda = 0.068$. Thus, for measurements in the vicinity of

the beam stop of scattering functions with weak curvature, such as radius of gyration measurements, the largest available wavelength spread, $\Delta\lambda/\lambda = 30\%$, is routinely used, particularly if the scattering is weak. On the other hand, as the distance R from the beam stop increases, the relative Q resolution, σ_Q/Q, decreases, asymptotically approaching σ_λ/λ [(3)]. Hence an effective strategy for measuring scattering that is sharply peaked at finite Q is to configure the instrument such that the peak occurs at large R and use a wavelength spread which is comparable to or less than $\Delta Q/Q_p$, where Q_p is the peak position and ΔQ is its width.

Finally, it should be noted that considerations other than detector count rate for a specific Q resolution may be used in selecting an instrument configuration, leading to somewhat different results. For example, requiring that a specific range of scattering vectors be measured with a specific resolution (Falcão et al., 1994; Margaça et al., 1991) leads to instrument configurations that are, in general, asymmetric ($L_1 \neq L_2$).

3.2. Flux at the sample

The flux at the sample position of the 30 m SANS instruments can vary by a factor of 10^4, depending on the guide configuration, wavelength and wavelength band. To measure the flux over this wide range, a cylindrical, 25.4 mm diameter, 607.95 kPa ^{3}He proportional counter (measured detection efficiency = 97.5% for 5 Å neutrons) was used in conjunction with a series of circular apertures, ranging in diameter from $\sim$1 to 15 mm, placed just in front of the counter at the sample position in order to keep the recorded count rate at a level where dead-time corrections were negligible. The aperture areas were calibrated by measuring the ratios of the count rates recorded for successive sizes using attenuators at the entrance of the instrument as needed to keep the count rate at an acceptable level (< 5000 s^{-1}). For the higher flux measurements, acrylic plastic sheets, the attenuation of which was independently calibrated for each wavelength, were used in combination with the apertures to keep the count rate below this level. Some results of flux measurements made at the sample position of the NG-3 SANS instrument, with the D_2O-ice cold source in operation, are summarized in Table 4 together with corresponding measured values for the LH_2 cold source. The flux measured at the sample position of the NG-3 SANS instrument is about 10–15% higher than the NG-7 SANS when no guides are used in the pre-sample flight. However, when all eight guide sections are used in the two instruments, the flux is about 30% higher at the sample position of the NG-3 instrument because in this condition the NG-3 SANS gains maximum benefit from having a larger guide (60 × 60 mm compared to 50 × 50 mm for NG-7) and a shorter gap (guide cut) where the velocity selector is located.

Table 4. *Flux at the sample for several configurations of the NG-3 SANS instrument with wavelength resolution,* $\Delta\lambda/\lambda = 0.15$, *and reactor power P = 20 MW*

The flux values for the D_2O-ice and LH_2 cold sources are measured values, as described in the text. The Q ranges given are for symmetric configurations of the instrument, $L_1 = L_2$, with the beam centered on the detector ($Q_{min} = 4\pi R_1/\lambda L_1$, $Q_{max} = \pi D/\lambda L_2$, where $D = 640$ mm is the detector size). Also listed are the diameters of the source and sample apertures, $2R_1$ and $2R_2$, respectively, and the number of 1.5 m long guide elements in the pre-sample flight path, N_g, which sets the source-to-sample distance L_1.

λ (nm)	$2R_1$ (mm)	$2R_2$ (mm)	N_g	$L_1 = L_2$ (m)	Q range (nm^{-1})	Flux† (cm^{-2} s^{-1})	Flux‡ (cm^{-2} s^{-1})
0.5	50	25	8	4	0.16–1.0	1.5×10^6	6.3×10^6
0.5	50	25	4	10	0.064–0.4	3.0×10^5	1.3×10^6
0.5	38	19	0	16	0.030–0.25	7.3×10^4	3.0×10^5
0.75	38	19	0	16	0.020–0.19	1.5×10^4	9.0×10^4
1.0	38	19	0	16	0.015–0.13	4.7×10^3	3.2×10^4

† Flux, measured for D_2O-ice cold source (effective Maxwellian temperature $\simeq 65$ K). ‡ Flux, measured for LH_2 cold source (effective Maxwellian temperature $\simeq 35$ K).

The measured neutron current (n s^{-1}) at the detector of the NG-3 30 m SANS instrument, with the reactor operating at 20 MW with its new liquid-hydrogen cold source, is plotted *versus* the Q range covered by the detector for several instrument configurations in Fig. 5. The quantity, I_d, plotted in the figure is the product of the flux at the sample, φ_s, the sample area, A_s, and the solid angle subtended by a detector element, $\Delta\Omega_d = (\Delta R/L_2)^2$, where $\Delta R = (3/2)^{1/2}(R_1/x)$ according to the optimization criteria in (5). For comparison, the shaded regions in Fig. 5 correspond to three configurations for the 80 m D11 SANS instrument at ILL, adapted from Lindner *et al.* (1992) as described in the figure caption. The count rates in the figure are proportional to the wavelength resolution, $\Delta\lambda/\lambda$, which is 0.09 for the D11 instrument and 0.15 for the NIST instrument. The detector on the NIST instrument covers a wider Q range because it can be offset up to 250 mm from the beam direction.

3.3. *Measurement methods*

3.3.1. *Sample transmission.* A measurement of the transmission of a sample, or the fraction of the incident beam that is not scattered in traversing the sample, is necessary both to correct the sample scattering for background and to determine the absolute differential scattering cross section. On the NIST SANS instruments, two methods are available to measure the transmission of a sample. A user may displace the beam stop in front of the area detector in order to measure the integrated intensity of the beam directly, provided an attenuator has been inserted at the entrance to the pre-sample flight path to reduce the intensity to a level (<100 counts s^{-1} pixel^{-1}) that is well below what is considered safe for the detector (< 1000 counts s^{-1} pixel^{-1} according to the manufacturer). The ratio of the detector count rate, integrated only over the area of the beam spot, with the sample in place, to that with nothing at the sample position ('empty beam') constitutes the transmission measurement. If the sample is

contained in a sample cell, a separate transmission measurement for an identical cell is performed, yielding T_c, in order to obtain the transmission of the sample itself, T_s, from the ratio of the two measurements, $T_s = T_{s+c}/T_c$. An advantage of this method is that any significant beam broadening due to multiple scattering or refraction in the sample, which renders the true transmission $T_s = 0$, can be detected from the observed beam profile.

Alternatively, the direct beam intensity may be sampled with a small detector installed on the main detector carriage which can be moved in front of the beam stop at the area detector when needed. The ratio of the count rate recorded on this detector (a 13 mm diameter × 100 mm long ^{3}He proportional counter with a 13 × 20 mm entrance slit for the beam) with and without the sample in position gives the sample transmission directly.

3.3.2. *Background and detector efficiency corrections.* Scattering data recorded on the area detector are corrected pixel by pixel for background according to the standard expression

$$I_s(i,j) = [I_{s+c}(i,j) - I_{bg}(I,j)] - (T_{s+c}/T_c)$$
$$\times [I_c(i,j) - I_{bg}(i,j)] \quad i,j = 1 \ldots 64 \quad (10)$$

where I_s is the net background-corrected scattering from the sample itself; I_{s+c} is the raw data from the sample (and its container, if not self-supporting); I_c is the intensity measured with only the sample container or nothing ('empty beam' run) at the sample position; and I_{bg} is the residual intensity (detector 'dark current') measured with the beam blocked at the sample position, ideally by covering the sample aperture with neutron-absorbing material. A measurement of I_c is necessary, in principle, even if no sample container is used in order to correct for parasitic scattering from beam windows, aperture edges, residual air in the flight path or spillage of the direct beam around the edge of the beam stop. Prior to performing the subtractions indicated in (10), each data-set is corrected for detector dead

time,† normalized to the same total number of beam monitor counts (to correct for differences in counting time and variations in the beam intensity during the measurements), and the counts in each pixel are divided by $\cos^3(\theta)$, where θ is the scattering angle, to correct for the small variation in solid angle subtended by a pixel because of the planar geometry of the detector.

The net scattering from the sample, I_s, is further corrected for nonuniformities in the detector efficiency by dividing, pixel by pixel, by the measured scattering from an isotropic scatterer such as water (Fig. 4). The isotropic scattering data are first normalized to 1 count pixel^{-1} and thus represent the point-to-point relative detector efficiency.

3.3.3. *Absolute intensity calibration.* The net scattering from the sample, after correcting for background and detector efficiency, $I_s(Q)$, expressed in counts per detector pixel per second, is related to the macroscopic cross section (cross section per unit volume) of the sample, $d\Sigma(Q)/d\Omega$, by the expression

$$I_s(Q) = \varphi_s A_s d_s T_{s+c}[d\Sigma(Q)/d\Omega]\Delta\Omega_d\varepsilon_d \qquad (11)$$

where $Q = (4\pi/\lambda)\sin(\theta/2)$ and the scattering angle $\theta = \arctan(R/L_2)$ where R is the radial distance of a pixel from the beam center position on the detector. The other factors in (11) are: the flux at the sample, φ_s; the area of the sample, A_s; the sample thickness, d_s; the transmission of the sample and its holder (if any), T_{s+c}; the absolute detector efficiency, ε_d; and the solid angle subtended by a detector pixel, $\Delta\Omega_d$. To determine the sample cross section, the (background-corrected) scattering from a standard sample, whose forward scattering cross section is known, is measured under identical instrument conditions. By dividing (11) by the corresponding expression for the scattering from the standard, the instrumental factors are eliminated to give

$$[d\Sigma(Q)/d\Omega] = [I_s(Q)/I_{std}(0)][(D_{std}T_{std})/(d_s T_{s+c})]$$
$$\times [d\Sigma_{std}(0)/d\Omega] \qquad (12)$$

where $I_{std}(0)$ is the measured scattering from the standard sample extrapolated to $Q = 0$, and d_{std}, T_{std} and $d\Sigma_{std}(0)/d\Omega$ are the thickness, transmission and forward scattering cross section, respectively, of the standard sample.

The samples used as intensity standards have strong forward scattering which can be measured to high precision relatively quickly (minutes, typically) and can be fitted to simple expressions, a Guinier law [ln(I) versus Q^2], for example, for reliable extrapolation to $Q = 0$. The cross sections of these standards are not assumed to be known from first principles (*i.e.* they are not primary standards), but are determined by measuring their scattering together with the instrumental factors in

(11). The product $(\varphi_s A_s\varepsilon_d)$ in (11) is determined by the same method described in §3.2 to determine the absolute flux at the sample, except that the SANS area detector is used rather than a ~100% efficient detector. The only other instrumental factor needed, $\Delta\Omega_d$, the solid angle subtended by a detector pixel, is computed from the detector distance and pixel size, $\Delta\Omega_d = 100 \text{ mm}^2/L_2^2$. The uncertainty in the cross sections determined by this procedure is estimated to be 5–10%.

Several samples are available to serve as convenient standards depending on the beam intensity and Q range covered for a particular SANS instrument configuration. The attributes of some of the samples currently used as intensity standards are listed in Table 5. The cross
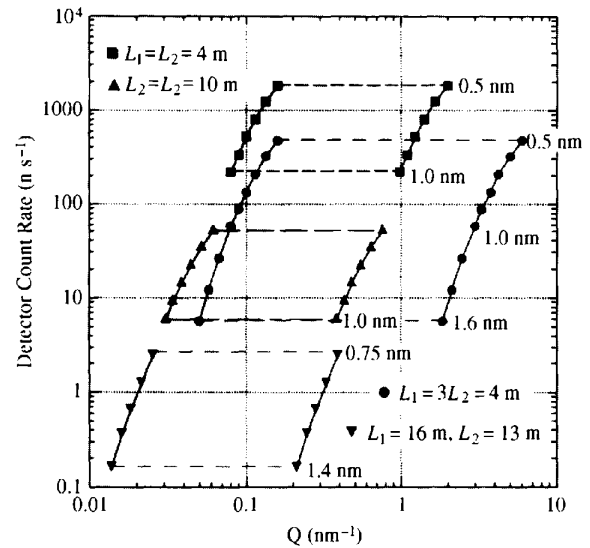

Fig. 5. The available Q range for several configurations of the NG-3 30 m SANS instrument. The ordinate, $I_d = \varphi_s A_s\Delta\Omega_d$, is the contribution to the scattering intensity (n s^{-1}) due to the instrument configuration (wavelength, wavelength resolution, detector position and collimation), where φ_s is the flux at the sample, $A_s = \pi(R_2)^2$ is the sample area, and $\Delta\Omega_d = (\Delta R/L_2)^2$ is the solid angle subtended by an area, ΔR^2, of the detector at distance L_2 from the sample. The values for I_d are calculated from measurements of the flux at the sample with the new LH_2 cold source (and reactor power $P = 20$ MW). For these computations, the source aperture radius, $R_1 = 25$ mm, with the sample radius, R_2, and the detector element dimension, ΔR, given by the relations in equations (5), *i.e.* $R_2 = R_1/(1 + x)$ and $\Delta R = (3/2)^{1/2}(R_1/x)$ where $x = L_1/L_2$. For comparison, I_d versus Q range for three symmetric configurations of the D11 SANS instrument at ILL is also shown by the three shaded regions where, from top to bottom, $L_1 = L_2 = 4.0$, 10.5 and 20.5 m, respectively. The data for D11 are adapted from Fig. 3 of Lindner *et al.* (1992) (which gives φ_s/L_2^2) by multiplying by the corresponding sample area, $A_s = 25 \times 15$ mm, and the same detector element area, $\Delta R^2 = 1.5R_1^2 = 940$ mm^2 used for the NG-3 SANS when $L_1 = L_2$. In addition, the Lindner *et al.* (1992) data have been multiplied by a factor of two to account for an improved velocity selector installed since then (Lindner, 1997). For D11, the wavelength resolution, $\Delta\lambda/\lambda = 0.09$, whereas $\Delta\lambda/\lambda = 0.15$ was used for the NG-3 SANS estimates. The wider Q range available for a given configuration of the NG-3 SANS instrument is the result of being able to offset the detector up to 250 mm from the beam axis.

---

† The counts recorded in each pixel are multiplied by the factor $(1 - N\tau)^{-1}$ where N is the total detector count rate and $\tau = 4$ µs is the measured dead time of the detector.

Table 5. *Samples used as cross-section calibration standards on the 30 m NIST SANS instruments*

The thickness of the samples (d_s) is 1.0 mm except where noted. The scattering from these samples, extrapolated to $Q = 0$ by fitting to functions and the Q range noted, determines the factor $I_{std}(0)$ used in equation (12) to calibrate the scattering from samples measured under identical conditions.

Standard sample	Cross section $d\Sigma(Q = 0)/d\Omega$ (cm^{-1})	Radius of gyration (Å)	Q range for fitting (Å^{-1})	Fitting function
Porous silica (SIL-A1)	26 (1)	31.5 (1.5)	0.02–0.04	$\ln(I)$ versus Q^2
Porous silica (SIL-A2)	28 (1)	31 (1.5)	0.02–0.04	$\ln(I)$ versus Q^2
Porous silica (SIL-B1)	57 (2)	58 (2)	0.01–0.025	$\ln(I)$ versus Q^2
Porous silica (SIL-B2)	54 (2)	58 (2)	0.01–0.025	$\ln(I)$ versus Q^2
Partially deuterated polyisoprene $X_D = 0.5$, MW = 70 K				
(POL-AS1)	66 (2)	75 (3)	≤ 0.01–0.03	Debye function (RPA approx.)
(POL-AS2)	64 (2)	76 (3)	≤ 0.01–0.03	Debye function (RPA approx.)
Partially deuterated polystyrene $X_D = 0.5$, MW = 200 K				
(POL-B1) (POL-B2) $d_s = 1.53$ mm	220 (15)	110 (5)	≤ 0.005–0.03	Debye function (RPA approx.)
Partially deuterated polystyrene $X_D = 0.5$, MW = 500 K				
(POL-C2) $d_s = 1.53$ mm	650 (3)	195 (10)	≤ 0.003–0.03	Debye function (RPA approx.)
Irradiated aluminium				
(Al -7) $d_s = 10.0$ mm	199 (6)	216 (4)	≤ 0.014	$\ln(I)$ versus Q^2

section obtained for the sample of irradiated single-crystal aluminium, designated Al-7 in Table 5, agrees well with that measured for this sample on the 30 m SANS facility at Oak Ridge National Laboratory (Wignall & Bates, 1987) at a wavelength of 4.75 Å.

The isotropic incoherent scattering from H_2O is often used as an absolute intensity calibrant at SANS facilities. However, even an H_2O sample should be considered as a secondary standard whose cross section must be carefully measured with reference to some primary standard on the particular SANS instrument on which it is to be used. Multiple scattering and inelastic scattering are considerable for even a 1 mm thick water sample and the exact contributions of these effects to the total measured scattering depends on the geometry of the sample (its diameter to thickness ratio) and the λ dependence of the detector efficiency, for example. Some of the difficulties in using water, or the incoherent scattering from vanadium, as an intensity standard are discussed in greater detail by Wignall & Bates (1987).

3.4. Instrument resolution function

If the Q dependence of the measured small-angle scattering is to be compared in detail with a scattering model or theory, it may be necessary to consider the effects of the instrument resolution function on the data. The resolution function, $R(\mathbf{Q} - \mathbf{Q}_o)$, is the probability that a neutron scattered with scattering vector $\mathbf{Q}$ is counted in a detector pixel corresponding to a nominal scattering vector $\mathbf{Q}_o$. The recorded detector counts represent a convolution of the scattering cross section for the sample with the resolution function which can distort or 'smear' the data.

The form of the resolution function for a pinhole-collimation SANS instrument with an area detector can be approximated using a bivariate Gaussian resolution function (Pedersen *et al.*, 1990). Following their convention, a Cartesian coordinate system is defined with components Q_1 and Q_2 parallel and perpendicular, respectively, to the nominal scattering vector $\mathbf{Q}_o$, as shown in Fig. 6. The variance of the resolution function in these two directions is given by

$$\sigma_{Q_1}^2 = k^2\{(1/4)(R_1/L_1)^2 + (R_2^2/4)[(1/L_1) + (1/L_2)]^2 + (\sigma_d/L_2)^2\} + Q_o^2(\sigma_\lambda/\lambda)^2$$

$$\sigma_{Q_2}^2 = k^2\{(1/4)(R_1/L_1)^2 + (R_2^2/4)[(1/L_1) + (1/L_2)]^2 + (\sigma_d/L_2)^2\}$$

(13)

where σ_d is the intrinsic spatial resolution of the detector [Δ_d (FWHM) = 2.355 σ_d = 10 mm for the NIST instruments]. The pinhole collimation gives a symmetrical contribution to the resolution function (in the Q_1, Q_2 coordinate system) whereas the wavelength spread produces an independent (*i.e.* uncorrelated) smearing in the magnitude of Q only. The bivariate resolution function is thus, in general, asymmetric, and can be expressed as

$$R(Q_o, Q_1, Q_2) = \{1/[\sigma_{Q_1}\sigma_{Q_2}(2\pi)^{1/2}]\}\exp\{-[(Q_1 - Q_o)^2 \times (2\sigma_{Q_1}^2)^{-1}] - (Q_2^2/2\sigma_{Q_2}^2)\}.$$

(14)

The importance of the wavelength spread in determining the shape of the resolution function is illustrated in Fig. 6 where half-height contours of the resolution function are plotted for several values of $\mathbf{Q}_o$. The

instrument parameters used in the calculation were: $L_1 = L_2 = 15$ m, $R_1 = 11$ mm, $R_2 = 6.0$ mm, $\sigma_d = 4.3$ mm, and either $\Delta\lambda/\lambda = 10\%$ (Fig. 6a) or 30% (Fig. 6b). These parameters represent the narrowest collimation available on the 30 m instruments and both the minimum and maximum wavelength spread.

For the detailed analysis of asymmetric SANS data, the bivariate form of the resolution function given in (14) should be used. For axially symmetric data, azimuthally averaging the bivariate resolution function

(a)

(b)
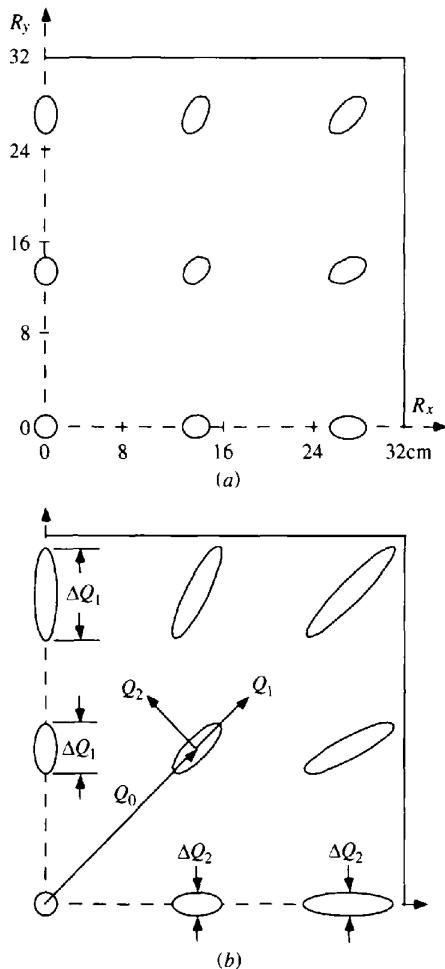
Fig. 6. Half-maximum contours of the bivariate Gaussian approximation for the resolution function of the 30 m SANS instruments at several points within one quadrant of the two-dimensional detector. The resolution function is circularly symmetric near the beam center ($Q = 0$) but becomes progressively elongated along the direction (Q_1) parallel to Q because of the wavelength spread in the beam. The FWHM values, ΔQ_1 and ΔQ_2, are calculated from the expressions in equation (13) (with $\Delta Q = 2.355\sigma_Q$). The instrument parameters used in the calculation were: $L_1 = L_2 = 15$ m, $R_1 = 11$ mm, $R_2 = 6.0$ mm, $\sigma_d = 4.3$ mm, and either $\Delta\lambda/\lambda = 10\%$ (Fig. 6a) or 30% (Fig. 6b). These parameters represent the narrowest collimation available on the 30 m instruments and both the minimum and maximum wavelength spread.

reduces to a simple Gaussian with a variance given by (3) and (4),† if second-order effects near the beam stop are ignored (Pedersen *et al.*, 1990; Barker & Pedersen, 1995).

3.5. Instrument performance

In this section, examples of data collected on the 30 m SANS instruments are presented to demonstrate various aspects of their actual performance.

3.5.1. *Beam profiles.* The shape and peak-to-background ratio of the profile of the incident beam at the area detector is one measure of the signal-to-noise of a SANS instrument and hence its sensitivity to weak scattering signals. Fig. 7 shows a typical beam profile for the NCNR's SANS instruments measured at a wavelength of 5 Å under the tightest collimation conditions (see figure caption) with the detector 13 m from the sample position. Under these conditions the neutron flux at the sample (for the NG-3 SANS instrument) is 9.9 $\times$ 10^4 cm^{-2}s^{-1} and the peak-to-background ratio, as seen in Fig. 7, is $> 10^6$ at the edge of the beam and $\sim 10^7$ over most of the detector.

3.5.2. *Polystyrene latex spheres.* The circularly averaged scattering from a nearly monodisperse dilute suspension of 100 nm diameter polystyrene latex spheres in D_2O is shown in Fig. 8. At this volume fraction (0.625%), the particles scatter independently. The data are, therefore, a direct measurement of the particle form factor (squared) for spheres convoluted with the instrumental resolution function and the narrow particle size distribution ($\sim 5\%$ standard deviation). The low-Q data, extending to a lower limit of 0.0013 Å^{-1}, were collected using 12 Å neutrons, the narrowest possible angular collimation, and a relaxed wavelength spread, $\Delta\lambda/\lambda$ (FWHM) = 30%, in order to maintain the count rate at an acceptable level (~ 100 counts s^{-1} measured over the whole detector when operating with the LH_2 cold source). To extend the measurements to larger Q, coarser collimation and a shorter wavelength, 7.5 Å, were used along with a narrower wavelength band, 10%, in order to resolve the characteristic oscillations that modulate the Q^{-4} asymptotic behavior of the form factor. The data from the two instrument settings appear to differ somewhat in their region of overlap. When corrections for instrumental resolution are made, however, agreement is much improved, as seen in the solid and dashed curves (shifted downward for clarity). These data demonstrate the low-Q limit of the 30 m SANS instruments as well as the versatility they provide to trade-off resolution *versus* intensity to meet the requirements of an experiment.

---

† In equation (4), the annular width, ΔR, is presumed to be much larger than the spatial resolution of the detector. σ_d (or Δ_d, the FWHM). If this is not the case, equation (4) should have an additional term, $1/12(\Delta_d/L_2)^2$.

3.5.3. *Nanocrystalline palladium.* The circularly averaged scattering from two small samples of nanocrystalline palladium, each 3 mm in diameter and 0.5 mm thick, is plotted in Fig. 9 (Sanders *et al.*, 1993). The material has an initial as-compacted grain size of about 50 Å and a bulk density of 86% of that of fully dense palladium. Despite the small sample size, data spanning eight orders of magnitude in intensity and nearly the entire Q range of the 30 m SANS instruments were collected using three instrument configurations (see figure caption for details). In the as-compacted sample, four distinct linear regions (in the log–log plot) can be identified which have been attributed to three sources of scattering. At the smallest Q, the -4-slope region is attributed to large voids, greater than 0.1 μm in size. The transition to a shallower slope followed by a second -4 slope, for Q between 0.005 and 0.1 Å^{-1}, is attributed to voids roughly the size of the grains. The leveling off of the scattering for $Q > 0.2$ Å^{-1} is attributed to entrapment of hydrogen during the powder fabrication process. Upon annealing (at 1073 K for 100 min), the missing grain-size voids are largely removed *via* sintering; the hydrogen diffuses out of the sample, while the large cavities remain largely intact.

3.5.4. *Ordered diblock copolymer micelles.* Fig. 10 is a gray-scale image of the scattering from an ordered solution of soft sphere polymer micelles in decane as recorded on the two-dimensional detector of the NG-7 SANS instrument (McConnell *et al.*, 1994). The micelles consist of diblock copolymers of perdeuterated polystyrene–polyisoprene (dPS–PI). In decane, a good solvent for PI but not for PS, the polymer chains self-

assemble to form spheres with a highly concentrated polystyrene core surrounded by a diffuse corona of polyisoprene. The data in Fig. 10 were obtained with the solution at rest after shearing at a low rate for a few
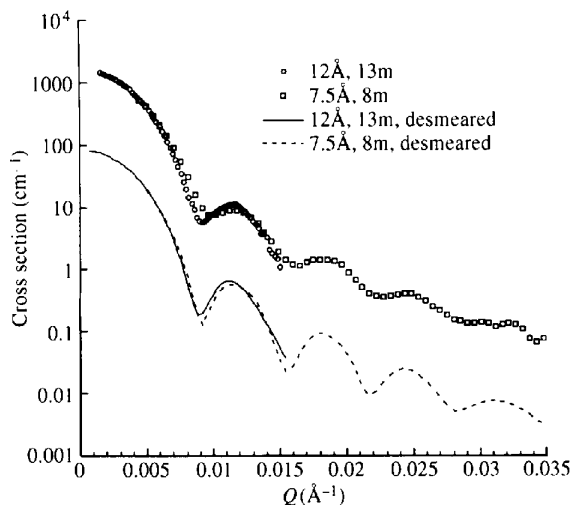
Fig. 8. The circularly averaged small-angle scattering from a nearly monodisperse dilute suspension of 100 nm diameter polystyrene latex spheres in D_2O measured on the NG-3 30 m SANS instrument (sample kindly provided by J. O'Reilly, Eastman Kodak). The low-Q data (open circles), extending to a lower limit of 0.0013 Å^{-1}, were collected in about 3 h with the following instrument configuration: λ = 12 Å; $\Delta\lambda/\lambda$ = 0.15; source-to-sample distance (L_1) = 16 m; sample-to-detector distance (L_2) = 13 m; source aperture diameter $2R_1$ = 22 mm; sample aperture diameter $2R_2$ = 13 mm. The larger-Q data (open squares) were collected in 30 min with: λ = 7.5 Å; $\Delta\lambda/\lambda$ = 0.10; $L_1 = L_2$ = 8 m; $2R_1$ = 50 mm; and $2R_2$ = 13 mm. Correcting for instrumental resolution (desmearing) results in the solid and dashed curves (shifted downward for clarity), for the 12 and 7.5 Å data-sets, respectively.
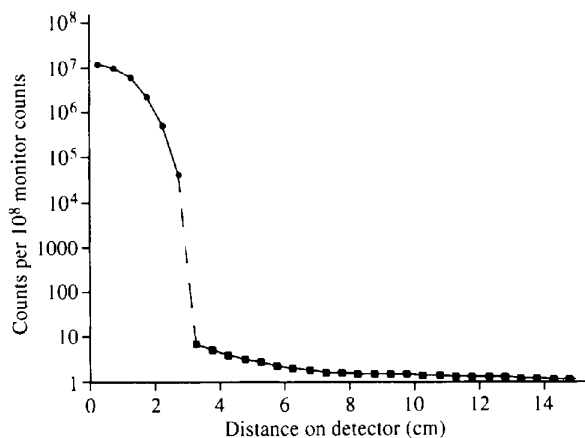

Fig. 7. The circularly averaged profile of the direct beam as recorded on the area detector of the NG-3 SANS instrument under the following conditions: source and sample aperture diameters of 25 and 13 mm, respectively, and a source-to-sample distance of 16 m; sample-to-detector distance of 13 m; 5.0 Å wavelength with $\Delta\lambda/\lambda$ = 15%. The dashed line is an interpolation between the central portion of the profile, measured with a calibrated attenuator in the beam and the beam stop removed, and the outer portion of the profile that was measured with no attenuation and a 50 mm diameter beam stop.
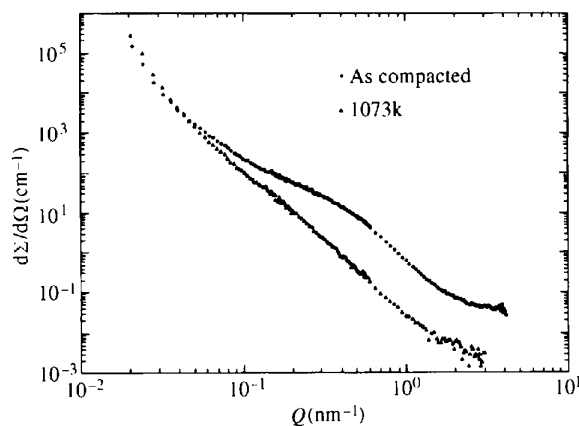

Fig. 9. Circularly averaged small-angle scattering from nanocrystalline palladium before and after annealing at 1073 K for 100 min. The data were acquired on the NG-3 30 m SANS instrument using 7.0 Å neutrons with a wavelength spread, $\Delta\lambda/\lambda$ = 0.30, and three sample-to-detector distances: L_2 = 12 m, for the data from ~0.002 to 0.028 Å^{-1} in scattering vector; L_2 = 5 m for the data from 0.014 to 0.07 Å^{-1}; and L_2 = 1.3 m for the data from 0.041 to 0.4 Å^{-1}.

minutes to induce ordering. The Bragg spots which result from the highly ordered face-centered-cubic structure of the micelles, analogous to structures commonly seen in charged-stabilized latex suspensions, are nearly resolution limited and manifest features of the instrument resolution function depicted in Fig. 6. The outer diffraction spots, for example, are elongated in the radial direction, similar to the resolution function contours shown in Fig. 6(a), because of the wavelength spread (10% FWHM) in the incident beam. The elongation is more pronounced in the spots in the upper half of Fig. 10. This was initially thought to be caused by additional spreading of the spots in the vertical direction as a result of gravity (which was not included in the calculated contours in Fig. 6a). However, gravity alone would tend to cause more spreading in the lower half of the image which is the opposite of what is observed. Hence this effect is presently not understood. Effects such as these may need to be considered in analyzing data like those in Fig. 10 in order to extract estimates of the degree of positional and orientational order in the sample, for example.

4. Further developments

The capability to carry out SANS measurements with polarized neutrons has recently been added to the NG-3 SANS instrument. A transmission polarizing cavity (Mezei, 1988), together with a flat coil spin flipper for reversing the direction of polarization, has been
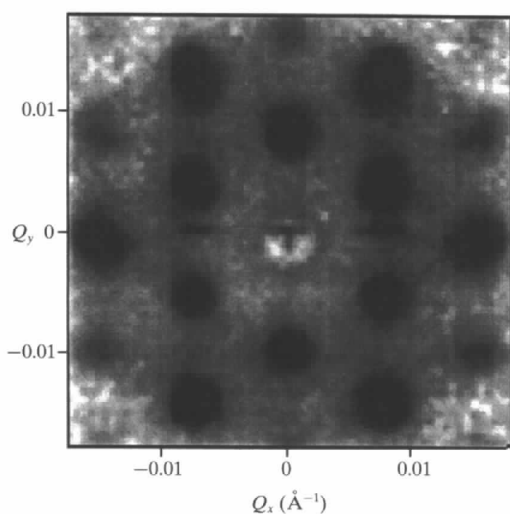

Fig. 10. A gray-scale image of the scattering (darker shading denotes higher scattered intensity) from an ordered solution of diblock copolymer micelles (perdeuterated polystyrene–polyisoprene) in decane as recorded on the two-dimensional detector of the NG-7 SANS instrument (McConnell et al., 1994). The data were collected using 7.0 Å neutrons, a wavelength spread $\Delta\lambda/\lambda = 10\%$ (FWHM) and a sample-to-detector distance of 15.85 m. The exact shapes of the diffraction spots on the detector are affected by the shape of the instrument resolution function (see Fig. 6).

installed on one of the moveable tables inside the pre-sample flight path for easy insertion when needed. The cavity consists of silicon plates with an Fe/Si supermirror coating which form a 'V' inside a section of copper-coated neutron guide. The cavity polarizes a wide beam (40×50 mm) over a range of wavelengths (5–15 Å) by preferentially reflecting neutrons of one spin state out of the beam.

5. Concluding remarks

The NIST 30 m SANS instruments are versatile, user-oriented instruments with a beam-flux and measurement range that are competitive with the best such instruments in the world. Up to 50% of the beam time on these instruments (75% on the NG-3 instrument and 25% on the NG-7 instrument) is available to any qualified researcher who submits an experiment proposal for external peer review.

References

Allemand, R., Bourdel, J., Roudaut, E., Convert, P., Ibel, K., Jacobé, J., Cotton, J. P. & Farnoux, B. (1975). *Nucl. Instrum. Methods*, **126**, 29–42.

Barker, J. G. & Pedersen, J. S. (1995). *J. Appl. Cryst.* **28**, 105–114.

Copley, J. R. D. (1993). *Nucl. Instrum. Methods Phys. Res. A*, **332**, 511–520.

Falcão, A. N., Pedersen, J. S. & Mortensen, K. (1994). *J. Appl. Cryst.* **27**, 330–337.

Glinka, C. J., Rowe, J. M. & LaRock, J. G. (1986). *J. Appl. Cryst.* **19**, 427–439.

Hammouda, B. (1992). *Nucl. Instrum. Methods Phys. Res. A*, **321**, 275–283.

Ibel, K. (1976). *J. Appl. Cryst.* **9**, 296–309.

Jacobe, J., Feltin, D., Rambaud, A., Ratel, J., Gamon, M. & Pernock, J. B. (1983). *Position-Sensitive Detection of Thermal Neutrons*, edited by P. Convert & J. B. Forsyth, pp. 106–119. London: Academic Press.

Lindner, P. (1997). Private communication.

Lindner, P., May, R. P. & Timmins, P. A. (1992). *Physica B*, **180–181**, 967–972.

McConnell, G. A., Gast, A. P., Huang, J. S., Lin, M. Y. & Smith, S. D. (1994). *Faraday Discuss. Chem. Soc.* **98**, 349.

Margaça, F. M. A., Falcão, A. N., Salgado, J. F. & Carvalho, F. G. (1991). *J. Appl. Cryst.* **24**, 994–998.

May, R. P. (1994). *J. Appl. Cryst.* **27**, 298–301.

Mezei, F. (1988). *Proc. Soc. Photo-Opt. Instrum. Eng.* **983**, 10–17.

Mildner, D. F. R. & Carpenter, J. M. (1984). *J. Appl. Cryst.* **17**, 249–256.

Pedersen, J. S., Posselt, D. & Mortensen, K. (1990). *J. Appl. Cryst.* **23**, 321–333.

Rosta, L., Zsigmond, G. Y., Farago, B., Mezei, F., Ban, K. & Perendi, J. (1987). KFKI Report 79E. Central Research Institute for Physics, Hungarian Academy of Sciences, Budapest.

Rosta, L. (1989). *Physica B*, **156–157**, 615–618

Sanders, P. G., Weertman, J. R., Barker, J. G. & Siegel, R. W. (1993). *Scr. Metall.* **29**, 91–96.

Schelten, J. (1972). *Kerntechnik*, **14**, 86–88.

Schmatz, W., Springer, T., Schelten, J. & Ibel, K. (1974). *J. Appl. Cryst.* **7**, 96–116.

Wignall, G. D. & Bates, F. S. (1987). *J. Appl. Cryst.* **20**, 28–40.